Kinematical error analysis and autonomous calibration of a 5PUS-RPUR parallel robot

Zesheng Wang[1,2], Yanbiao Li[3], Bo Chen [3]*, Kexin Ding[1], Jialong Zhu[1], Min Zhuang[1]

1 School of Intelligent Manufacturing, Hangzhou Polytechnic, Hangzhou, China, **2** State Key Laboratory of Fluid Power and Mechatronic Systems, Zhejiang University, Hangzhou, China, **3** College of Mechanical Engineering, Zhejiang University of Technology, Hangzhou, China

* chenb@zjut.edu.cn

Abstract

Kinematic calibration is essential for improving the absolute accuracy of parallel robots, but conventional identification methods often struggle with the complex, non-linear coupling of their numerous geometric error parameters. This can lead to convergence to local rather than global optima, limiting the effectiveness of the calibration. To address this challenge, this paper proposes a novel self-calibration methodology based on a global optimization strategy. Taking the 5PUS-RPUR parallel robot as an example, its inverse kinematics is established based on screw theory. A sensitivity analysis is performed using the finite difference method to screen for and eliminate error sources with a negligible impact on the moving platform's pose. Measurement points are then selected uniformly throughout the workspace using the farthest point sampling algorithm. An objective function for the GA is constructed by integrating the actuator displacement errors from each kinematic chain with the overall pose error of the moving platform. Non-linear constraints are handled using a penalty function approach. Based on measurement data from an onboard IMU and joint encoders, the identification results are obtained. The experimental results demonstrate that the proposed method significantly improves the robot's positional accuracy across its entire workspace. The superiority and efficacy of this approach are further corroborated by a benchmark comparison with three recent, state-of-the-art calibration methodologies.

1. Introduction

Lower-mobility parallel robots offer advantages such as simpler architecture and lower costs in design, control, and manufacturing compared to their 6-DOF counterparts [1]. They are well-suited for numerous tasks requiring fewer than six DOFs in industrial and medical applications [2]. For instance, 3T2R motion capabilities cover a wide range of applications, including 5-axis machining [3,4], welding [5], and surgical procedures [6]. However, physical robots are unavoidably subject to geometric

imperfections, such as manufacturing tolerances and link misalignments, which cause significant discrepancies between the commanded and the actual end-effector pose. Calibration offers a powerful and cost-effective method to compensate for these deviations through software, thereby enhancing pose accuracy without requiring expensive improvements in manufacturing precision [7–9].

Kinematic calibration generally involves four key steps: error modeling, measurement, parameter identification, and compensation [10]. First, an error model is formulated to relate the robot's nominal kinematics to its actual behavior, typically using data from internal or external sensors. Based on this model, a parameter identification process is then performed to quantify the geometric errors [11–13]. Subsequently, the identified parameters are used to modify the controller model, thereby improving the pose accuracy of the parallel robot [14,15]. However, the large number of error parameters and their complex, non-linear coupling in parallel robots significantly complicate the identification process. To address these challenges, numerous researchers have explored advanced identification strategies, motivating the work presented in this paper. Luo et al. [16] developed a kinematic model for a novel 4PPa-2PaR parallel manipulator that incorporates its non-ideal geometric parameters. They employed the Levenberg-Marquardt (LM) algorithm to identify 10 key error parameters, with the objective of minimizing the error in each individual kinematic chain. After calibration, the average pose accuracy of the moving platform was greatly improved. Song et al. [17] proposed a robust calibration method for joint compensation based on an artificial neural network (ANN). Taking a Stewart platform as their case study, they set the minimization of individual kinematic chain errors as the optimization objective. The calibration experiments demonstrated a 91.90% reduction in the mean position error and a 90.22% reduction in the mean posture error. Gao et al. [18] established a linear error model for individual kinematic chains with the objective of minimizing inverse kinematic residuals. By combining full-pose measurements with actuator displacement data, they employed an iterative linear least-squares method for parameter identification. This approach reduced the pose error from 8 mm/ 0.4° before calibration to 0.4 mm/ 0.04° after calibration. Using screw theory, Sun et al. [19] established a comprehensive error model that included 18 geometric error sources of a 3-DoF rotational parallel manipulator. They then solved the error equation for each individual chain by combining Tikhonov regularization with the Generalized Cross-Validation (GCV) method for optimal parameter identification. Post-calibration results showed an improvement in orientation accuracy of over 53.4%. Zhang et al. [20] constructed a non-linear error model for the individual chains of a Stewart platform using closed-loop vector constraints. They employed the LM algorithm to solve the resulting non-linear least-squares problem. The experimental results demonstrated a significant improvement in accuracy: the position error was reduced from the millimeter level to within ±0.2 mm, while the orientation accuracy improved by an order of magnitude compared to the uncalibrated system. He et al. [21] presented a calibration methodology for a 7-DOF UP&2UPS-4R hybrid manipulator. A comprehensive error model was established by treating the parallel mechanism as an equivalent serial chain. An iterative least-squares method was employed

to identify the kinematic parameter errors. This approach reduced the average error of the hybrid manipulator by 85%, significantly enhancing its kinematic accuracy. Existing strategies for error parameter identification, however, possess certain limitations. While optimization algorithms such as gradient descent, the Newton-Raphson method, and least-squares are computationally efficient, they typically employ an independent chain optimization strategy. This approach can only guarantee a local optimum for each individual kinematic chain, as it neglects the mutual constraint relationships between them. Consequently, the overall calibration result may deviate significantly from the global optimum.

Due to the high-order non-linearities and strong coupling among the various chain error parameters, obtaining an explicit mathematical model of their interdependencies is exceedingly difficult. This limitation necessitates an optimization approach capable of navigating the complex solution space without relying on a predefined coupling model. To this end, we turn to the Genetic Algorithm (GA), a metaheuristic renowned for its powerful global search capabilities and its adeptness at handling non-linear, multi-modal problems. The GA has demonstrated significant success in diverse fields such as the optimal allocation of electric vehicle charging stations [22], mobile robot path planning [23], and aircraft mission planning [24]. To achieve a globally optimal calibration for the parallel robot, we design a weighted fitness function that fuses the actuator displacement errors from individual chains with the overall pose error of the robot's end-effector. This function, serving as the GA's optimization objective, simultaneously evaluates the contribution of all chains to the end-effector accuracy during the optimization process. It thereby compels the algorithm to find a parameter set that holistically coordinates error compensation across the entire robot, fundamentally circumventing the issue of explicit parameter coupling and achieving a truly global optimum.

This paper presents the error modeling and kinematic calibration of a five degree-of-freedom 5PUS-RPUR (R, P, S, and U stand for revolute, prismatic, spherical, and universal joints) parallel robot, with the implementation by the following steps: (1) formulation of the inverse kinematics by integrating screw theory, Paden–Kahan (PK) subproblems and the elimination method; (2) error modeling within the screw theory framework and global sensitivity analysis of the influence of the geometric variations onto the moving platform pose; (3) identification of geometric parameters by pose measurement using a IMU and encoder. With the objective function that integrates individual chain actuator errors with the end-effector pose error, the parameter identification is realized by solving an unconstrained nonlinear optimization problem via GA. After calibration, the position error of the moving platform is significantly improved throughout the operational workspace.

2. Analysis of inverse kinematics

The inverse kinematics problem involves determining the required actuator displacements to achieve a desired end-effector pose. While a common approach for this analysis is to combine screw theory with Paden-Kahan (PK) subproblems, this method is not directly applicable to the 5PUS-RPUR robot, specifically for the inverse kinematics of its RPUR chain. To address this limitation, the elimination method is used to reduce the unknown parameters in the pose analysis of the RPUR chain.

There are three recognized basic PK subproblems [25]. For the inverse position analysis of the 5PUS-RPUR parallel robot, the solution does not involve PK subproblems 3. This study only clarifies the first two recognized subproblems. PK subproblem 1 is shown in Fig 1(a), the spatial point p_1 rotates around the fixed axis ξ to the given point p_2, and r is a point on the axis ξ. θ is the rotation angle to be calculated.

$$\begin{cases} \theta = \text{atan2}\left(\xi^{\mathrm{T}}\left(u' \times v'\right), u'^{\mathrm{T}}v'\right) \\ u' = u - \xi\xi^{\mathrm{T}}u \\ v' = v - \xi\xi^{\mathrm{T}}v \end{cases} \tag{1}$$

PK subproblem 2 is shown in Fig 1(b), the spatial point p_1 rotates around axis ξ_2 and axis ξ_1 to the given point p_3, respectively, and θ_1 and θ_2 are the rotation angles to be calculated.
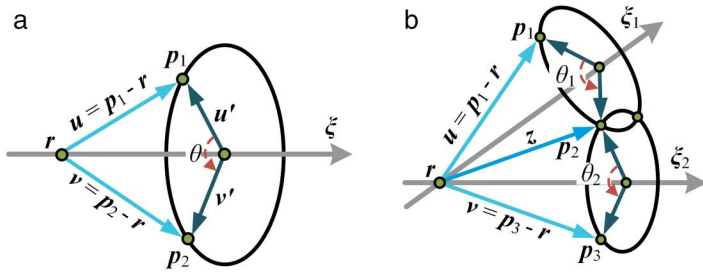
Fig 1. The two recognized basic PK sub-problems. (a) PK sub-problem 1. **(b)** PK sub-problem 2.

https://doi.org/10.1371/journal.pone.0330675.g001

$$\begin{cases} \boldsymbol{z} = \iota_1 \boldsymbol{\xi}_1 + \iota_2 \boldsymbol{\xi}_2 + \iota_3 \left(\boldsymbol{\xi}_1 \times \boldsymbol{\xi}_2 \right) \\ \iota_1 = \dfrac{(\boldsymbol{\xi}_1^{\mathsf{T}} \boldsymbol{\xi}_2) \boldsymbol{\xi}_2^{\mathsf{T}} \boldsymbol{u} - \boldsymbol{\xi}_1^{\mathsf{T}} \boldsymbol{v}}{\left(\boldsymbol{\xi}_1^{\mathsf{T}} \boldsymbol{\xi}_2 \right)^2 - 1}, \iota_2 = \dfrac{(\boldsymbol{\xi}_1^{\mathsf{T}} \boldsymbol{\xi}_2) \boldsymbol{\xi}_1^{\mathsf{T}} \boldsymbol{v} - \boldsymbol{\xi}_2^{\mathsf{T}} \boldsymbol{u}}{\left(\boldsymbol{\xi}_1^{\mathsf{T}} \boldsymbol{\xi}_2 \right)^2 - 1} \\ \iota_3^2 = \dfrac{\|\boldsymbol{u}\|^2 - \iota_1^2 - \iota_2^2 - 2\iota_1 \iota_2 \boldsymbol{\xi}_1^{\mathsf{T}} \boldsymbol{\xi}_2}{\|\boldsymbol{\xi}_1 \times \boldsymbol{\xi}_2\|^2} \end{cases} \tag{2}$$

In addition to the known P-K sub-problems, a novel kind of subproblem 3 is encountered in our problem. As shown in Fig 2, the spatial point $\boldsymbol{p}_1$ moves along the axis $\boldsymbol{\xi}_1$ by a distance θ_1 to the given point $\boldsymbol{p}_2$, the distance between position vectors $\boldsymbol{p}_2$ and $\boldsymbol{p}_3$ is given as δ. The unknown parameter θ_1 can be formulated as

$$\begin{cases} \theta_1 = \|\boldsymbol{v}\| \cos \theta_0 + \delta' \\ \boldsymbol{v} = \boldsymbol{p}_3 - \boldsymbol{p}_1, \cos \theta_0 = \left(\dfrac{\boldsymbol{\xi}^{\mathsf{T}} \boldsymbol{v}}{\|\boldsymbol{v}\|} \right) \\ \delta'^2 = \left(\|\boldsymbol{v}\| \cos \theta_0 \right)^2 - \left(\|\boldsymbol{v}\|^2 - \delta^2 \right) \end{cases} \tag{3}$$

where if $\delta'^2 = 0$, there will be one solution for subproblem 3, and vector $\boldsymbol{p}_3 - \boldsymbol{p}_1$ is perpendicular to vector $\boldsymbol{\xi}_1$; else if $\delta'^2 > 0$, two solutions exist while position vectors $\boldsymbol{p}_2$ and $\boldsymbol{p}'_2$ lie on opposite sides of the perpendicular line to vector $\boldsymbol{\xi}_1$. Otherwise, no solution exists. In particular, when point $\boldsymbol{p}_3$ is on axis $\boldsymbol{\xi}_1$, then $\theta_1 = (\boldsymbol{p}_3 - \boldsymbol{p}_1)^{\mathsf{T}} \boldsymbol{\xi}_1 - \delta$.

2.1. Structure of the 5PUS-RPUR parallel robot

The virtual prototype of the 5PUS-RPUR parallel robot is shown in Fig. 3a, which consists of a base, a moving platform, and two types of serial PUS and RPUR chains. The PUS chain contains a prismatic joint (P) comprised of a module, a side plate and a slider, a universal joint (U1) and a spherical joint (S), where U and S are connected by the fixed-length rod. The RPUR chain consists of two revolute joints (R), a prismatic joint composed of an electric cylinder and a push rod, a universal joint (U2) and a fixed-length rod, where the first revolute joint (R1) is directly connected to the base and the second revolute joint (R2) is connected to the universal joint via the fixed-length rod.

As shown in Fig. 3b, the kinematic screws of each branch chain are established in the static coordinate system. The screw of the P joint in the PUS chain is along its motion direction, and the U joint is decomposed into two R joints, with the twists of the R joints along their rotation axis directions. The S joint is decomposed into three R joints, one along the direction of the fixed-length rod A_iB_i, and the other two are parallel to the X and Y axes of the static coordinate system when its Z-axis is rotated to align to the direction of A_iB_i. For the RPUR chain, the universal joint is decomposed into two R joints, with screw directions parallel to the X axis of the static coordinate system and the Y axis of the moving coordinate system. The screw directions of the other two R joints are both along their axial directions. The screw direction of the P joint is parallel to the z-axis direction.
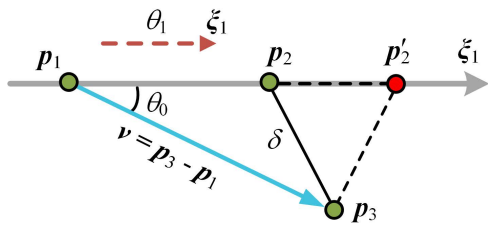
Fig 2. PK subproblem 3.
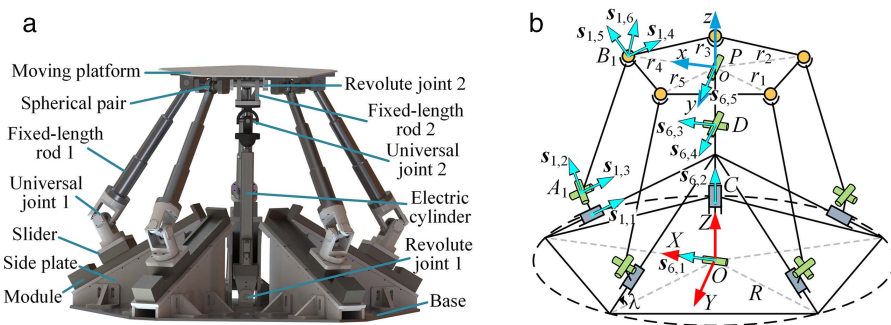
Fig. 3. Virtual prototype and kinematic screw system of the 5PUS-RPUR parallel robot. (a) Virtual prototype. (b) Kinematic screw system.

2.2. Inverse displacement analysis of the PUS chain

In terms of the joint connection form of the PUS chain, the pose of the center point on the moving platform can be expressed as

$$\boldsymbol{g}_i(\theta) = \prod_{j=1}^{5} \exp\left(\hat{\xi}_{i,j}, \theta_{i,j}\right) \cdot \boldsymbol{g}_i(0), i = 1 \sim 5 \tag{4}$$

where $\exp(\cdot)$ is the product of exponential formula [26]. i and j are the indices for the kinematic chain and the joint within that chain, respectively. $\boldsymbol{g}_i(0)$ and $\boldsymbol{g}_i(\theta)$ represent the initial and desired pose of the moving platform. $\theta_{i,j}$ and $\hat{\xi}_{i,j}$ ($j = 1 \sim 6$) denote the displacement and the kinematic screw of each branch joint.

Since the posterior three joint axes of the PUS chain intersect with a point B_i, the following formula can be obtained according to the principle of position invariance.

$$\exp(\hat{\xi}_{i,4}, \theta_{i,4}) \cdot \exp(\hat{\xi}_{i,5}, \theta_{i,5}) \cdot \exp(\hat{\xi}_{i,6}, \theta_{i,6}) \cdot \boldsymbol{P}_{Bi} = \boldsymbol{P}_{Bi} \tag{5}$$

with $\boldsymbol{P}_{Bi} = [\boldsymbol{p}_{Bi} \ 1]^{\mathrm{T}}$, $\boldsymbol{p}_{Bi}$ denotes the position vector of the point B_i.

Taking the right multiplication for Eq. (4) with the inverse matrix $\boldsymbol{g}_i^{-1}(0)$ and matrix $\boldsymbol{P}_{Bi}$, Eq. (4) can be rewritten as

$$\boldsymbol{g}_i(\theta)\boldsymbol{g}_i^{-1}(0)\boldsymbol{P}_{Bi} = \exp(\hat{\xi}_{i,1}, \theta_{i,1}) \cdot \exp(\hat{\xi}_{i,2}, \theta_{i,2})\exp(\hat{\xi}_{i,3}, \theta_{i,3})\boldsymbol{P}_{Bi} \tag{6}$$

Similarly, due to the last two joints in the first three joints converging at a point A_i, it can be obtained from the principle of position invariance.

$$\exp(\hat{\xi}_{i,2}, \theta_{i,2}) \cdot \exp(\hat{\xi}_{i,3}, \theta_{i,3}) \cdot \boldsymbol{P}_{Ai} = \boldsymbol{P}_{Ai} \tag{7}$$

with $\boldsymbol{P}_{Ai} = [\boldsymbol{p}_{Ai}\ 1]^{\mathsf{T}}$, $\boldsymbol{p}_{Ai}$ denotes the position vector of the point A_i.

Taking the left dot product of Eq. (7) with $\exp(-\hat{\xi}_{i,1}, \theta_{i,1})$, we get

$$\exp(-\hat{\xi}_{i,1}, \theta_{i,1})\boldsymbol{g}_i(\theta)\boldsymbol{g}_i^{-1}(0)\,\boldsymbol{P}_{Bi} = \exp(\hat{\xi}_{i,2}, \theta_{i,2})\exp(\hat{\xi}_{i,3}, \theta_{i,3})\boldsymbol{P}_{Bi} \tag{8}$$

Subtracting the matrix $\boldsymbol{P}_{Ai}$ on both sides of Eq. (8), we obtain

$$\exp(-\hat{\xi}_{i,1}, \theta_{i,1})\boldsymbol{g}_i(\theta)\boldsymbol{g}_i^{-1}(0)\,\boldsymbol{P}_{Bi} - \boldsymbol{P}_{Ai} = \exp(\hat{\xi}_{i,2}, \theta_{i,2})\exp(\hat{\xi}_{i,3}, \theta_{i,3})\,(\boldsymbol{P}_{Bi} - \boldsymbol{P}_{Ai}) \tag{9}$$

According to the principle of distance invariance [27], it is easy to obtain

$$\left|\boldsymbol{P}_{Bi} - \boldsymbol{P}_{Ai}\right| = \left|\exp(\hat{\xi}_{i,2}, \theta_{i,2})\exp(\hat{\xi}_{i,3}, \theta_{i,3})\,(\boldsymbol{P}_{Bi} - \boldsymbol{P}_{Ai})\right| \tag{10}$$

Substituting Eq. (10) into Eq. (9) shows that it corresponds to PK subproblem 3, and its parameters are expressed as follows.

$$\begin{cases} \hat{\xi} = -\hat{\xi}_{i,1}^{\mathsf{T}}, \boldsymbol{p}_1 = \boldsymbol{g}_i(\theta)\boldsymbol{g}_i^{-1}(0)\,\boldsymbol{P}_{Bi} \\ \boldsymbol{v} = \boldsymbol{P}_{Ai} - \boldsymbol{p}_1, \delta^2 = \|\boldsymbol{P}_{Bi} - \boldsymbol{P}_{Ai}\|^2 \end{cases} \tag{11}$$

It is worth noting that the prismatic pair can be regarded as the revolute pair of the rotational axis at infinity. Substituting the parameters into PK subproblem 3, the analytical expression of $\theta_{i,1}$ can be derived.

On the basis of the known $\theta_{i,1}$, Eq. (9) can be regarded as PK subproblem 2, and the corresponding subproblem parameters are expressed as follows.

$$\begin{cases} \boldsymbol{\xi}_1 = \hat{\xi}_{i,2}, \ \boldsymbol{\xi}_2 = \hat{\xi}_{i,3}, \boldsymbol{u} = \boldsymbol{P}_{Bi} - \boldsymbol{P}_{Ai} \\ \boldsymbol{v} = \exp(-\hat{\xi}_{i,1}, \theta_{i,1})\boldsymbol{g}_i(\theta)\boldsymbol{g}_i^{-1}(0)\,\boldsymbol{P}_{Bi} - \boldsymbol{P}_{Ai} \end{cases} \tag{12}$$

where the analytical expressions for $\theta_{i,2}$ and $\theta_{i,3}$ can be solved from the PK subproblem 2.

Substituting the equation $\exp(\hat{\xi}_{i,6}, \theta_{i,6})\boldsymbol{P}_{Ai} = \boldsymbol{P}_{Ai}$ into Eq. (4), which can be rewritten as

$$\begin{aligned} \exp(\hat{\xi}_{i,4}, \theta_{i,4})\exp(\hat{\xi}_{i,5}, \theta_{i,5})\,(\boldsymbol{P}_{Bi} - \boldsymbol{P}_{Ai}) = \exp(-\hat{\xi}_{i,3}, \theta_{i,3}) \\ \exp(-\hat{\xi}_{i,2}, \theta_{i,2})\exp(-\hat{\xi}_{i,1}, \theta_{i,1})\boldsymbol{g}_i(\theta)\boldsymbol{g}_i^{-1}(0)\,(\boldsymbol{P}_{Bi} - \boldsymbol{P}_{Ai}) \end{aligned} \tag{13}$$

where the vector $\boldsymbol{P}_{Ai}$ should be selected on the axis $\hat{\xi}_{i,6}$ and not on the axes $\hat{\xi}_{i,4}$ and $\hat{\xi}_{i,5}$. On the basis of the known $\hat{\xi}_{i,1}$, $\hat{\xi}_{i,2}$ and $\hat{\xi}_{i,3}$, the analytical expressions of $\theta_{i,4}$ and $\theta_{i,5}$ can be solved by using the inverse solution formula of PK subproblem 2.

Multiplying Eq. (5) on the left by $\exp(-\hat{\xi}_{i,5}, \theta_{i,5})\cdots\exp(-\hat{\xi}_{i,1}, \theta_{i,1})$ and on the right by $\boldsymbol{g}_i^{-1}(0)\cdot{}^A\boldsymbol{p}$, we can obtain

$$\exp(\hat{\xi}_{i,6}, \theta_{i,6}) \cdot {}^A\boldsymbol{p} = \exp(-\hat{\xi}_{i,5}, \theta_{i,5})\cdots\exp(-\hat{\xi}_{i,1}, \theta_{i,1}) \cdot \boldsymbol{g}_i(\theta) \cdot \boldsymbol{g}_i^{-1}(0) \cdot {}^A\boldsymbol{P} \tag{14}$$

where ${}^A\boldsymbol{P} = [{}^A\boldsymbol{p}\ 1]^{\mathsf{T}}$, ${}^A\boldsymbol{p}$ is the position vector of any spatial point not on the rotational axis. The analytical expression of $\theta_{i,6}$ can be solved by using the inverse solution formula of PK subproblem 1.

2.3. Inverse displacement analysis of the RPUR chain

In terms of the structural form of the RPUR chain, the pose of the center point on the moving platform can be expressed as

$$\boldsymbol{g}_i(\theta) = \exp\left(\hat{\boldsymbol{\xi}}_{i,1}, \theta_{i,1}\right) \cdot \exp\left(\hat{\boldsymbol{\xi}}_{i,2}, \theta_{i,2}\right) \cdot \exp\left(\hat{\boldsymbol{\xi}}_{i,3}, \theta_{i,3}\right) \cdot \exp\left(\hat{\boldsymbol{\xi}}_{i,4}, \theta_{i,4}\right) \cdot \exp\left(\hat{\boldsymbol{\xi}}_{i,5}, \theta_{i,5}\right) \cdot \boldsymbol{g}_i(0) , i = 6 \tag{15}$$

where $\hat{\boldsymbol{\xi}}_{i,j}$ and $\theta_{i,j}$ $(j = 1 \sim 5)$ represent the joint kinematic screw and joint displacement of the RPRU chain.

Expanding Eq. (15) and taking the first-row matrix from both sides, we obtain

$$\begin{bmatrix} \cos(\beta)\cos(\gamma) & -\cos(\beta)\sin(\gamma) & \sin(\beta) & x \end{bmatrix} = \begin{bmatrix} \cos(\theta_{i,4} + \theta_{i,5}) & 0 & \sin(\theta_{i,4} + \theta_{i,5}) & \sin(\theta_{i,4}) h_0 \end{bmatrix} \tag{16}$$

with $\boldsymbol{g}_i(\theta) = \begin{bmatrix} \boldsymbol{R}x(\alpha)\boldsymbol{R}y(\beta)\boldsymbol{R}z(\gamma) & \boldsymbol{p} \\ \boldsymbol{0}_{1\times3} & 1 \end{bmatrix}$, $\boldsymbol{p} = \begin{bmatrix} x & y & z \end{bmatrix}^{\mathsf{T}}$,

where α, β and γ represent the Euler rotation angles of the moving platform around the x, y and z axes of the moving coordinate system. $\boldsymbol{p}$ denotes the position vector of the reference point on the moving platform. h_0 is the distance from the center of U2 to the origin of the moving coordinate system. According to Eq. (16), $\gamma = 0$. This indicates that the 5PUS-RPUR parallel robot has the motion characteristic with three-dimensional positional movement and two-dimensional Eulerian angular rotation.

In terms of Eq. (16), the relationship between joint angle displacements $\theta_{i,4}$ and $\theta_{i,5}$ as well as the pose of the moving platform can be obtained.

$$\begin{cases} \theta_{i,4} = \arcsin\left(\frac{x}{h_0}\right) \\ \theta_{i,5} = \beta - \theta_{i,4} \end{cases} \tag{17}$$

where the expressions of joint angles $\theta_{i,4}$ and $\theta_{i,5}$ are obtained using the elimination method. Taking the right multiplication for both sides of Eq. (15) with the vector $\boldsymbol{P}_D$, it can be obtained based on the principle of distance invariance.

$$\exp(\hat{\boldsymbol{\xi}}_{i,1}, \theta_{i,1}) \cdot \exp(\hat{\boldsymbol{\xi}}_{i,2}, \theta_{i,2}) \cdot \boldsymbol{P}_D = \boldsymbol{g}_i(\theta) \cdot \boldsymbol{g}_i^{-1}(0) \cdot \exp(\hat{\boldsymbol{\xi}}_{i,5}, -\theta_{i,5}) \cdot \exp(\hat{\boldsymbol{\xi}}_{i,4}, -\theta_{i,4}) \cdot \boldsymbol{P}_D \tag{18}$$

where $\boldsymbol{P}_D$ denotes the position vector of the center of universal joint 2.

Due to the distance from the center of U to the origin of the static coordinate system is not affected by R2, the joint displacement $\theta_{i,2}$ can be solved by PK subproblem 3, and the subproblem parameters are expressed as

$$\begin{cases} \boldsymbol{p}_1 = \boldsymbol{p}_U, \boldsymbol{p}_3 = \boldsymbol{p}_O, \boldsymbol{\xi} = \hat{\boldsymbol{\xi}}_{i,2}, \\ \delta = \left\| \boldsymbol{g}_i(\theta)/\boldsymbol{g}_i(0) \exp(\hat{\boldsymbol{\xi}}_{i,5}, -\theta_{i,5})\exp(\hat{\boldsymbol{\xi}}_{i,4}, -\theta_{i,4})\boldsymbol{P}_D - \boldsymbol{P}_O \right\| \end{cases} \tag{19}$$

where $\boldsymbol{P}_o = [\boldsymbol{p}_o \ 1]^{\mathsf{T}}$, $\boldsymbol{p}_o$ is the position vector of the origin of the moving coordinate system.

On the basis of the known joint displacements $\theta_{i,2}$, $\theta_{i,4}$ and $\theta_{i,5}$, the analytical expression of the joint angle $\theta_{i,1}$ can be obtained by converting Eq. (18) to PK subproblem 1, and the subproblem parameters are expressed as

$$\begin{cases} \boldsymbol{r} = \boldsymbol{p}_O, \hat{\boldsymbol{\xi}} = \hat{\boldsymbol{\xi}}_{i,1}, \boldsymbol{P}_1 = \exp(\hat{\boldsymbol{\xi}}_{i,2}, \theta_{i,2}) \cdot \boldsymbol{P}_D, \\ P_2 = \boldsymbol{g}_i(\theta)/\boldsymbol{g}_i(0) \cdot \exp(\hat{\boldsymbol{\xi}}_{i,5}, -\theta_{i,5}) \cdot \exp(\hat{\boldsymbol{\xi}}_{i,4}, -\theta_{i,4}) \cdot \boldsymbol{P}_D \end{cases} \tag{20}$$

where $\boldsymbol{p}_1$ and $\boldsymbol{p}_2$ are matrices consisting of the first three columns of elements of matrices $\boldsymbol{P}_1$ and $\boldsymbol{P}_2$. $\boldsymbol{P}_D = [\boldsymbol{p}_D \ 1]^{\mathsf{T}}$, $\boldsymbol{p}_D$ is the position vector of the U center in the RPRU chain.

Likewise, the explicit expressions of joint displacements $\theta_{i,3}$ can be analyzed by Eq. (15) equivalent to PK subproblem 1, and the subproblem parameters are expressed as

$$\begin{cases} \boldsymbol{r} = \boldsymbol{p}_D, \hat{\xi} = \hat{\xi}_{i,3}, \boldsymbol{p}_1 = \boldsymbol{p}_O \\ \boldsymbol{p}_2 = \exp(\hat{\xi}_{i,2}, \theta_{i,2}) \cdot \exp(\hat{\xi}_{i,1}, \theta_{i,1}) \cdot \boldsymbol{g}_i(\theta) \cdot \boldsymbol{g}_i^{-1}(0) \cdot \exp(\hat{\xi}_{i,5}, -\theta_{i,5}) \cdot \exp(\hat{\xi}_{i,4}, -\theta_{i,4})\boldsymbol{P}_O \end{cases} \tag{21}$$

At this point, the analytical formulas of each branched chain joint have been obtained. It should be noted that there will be generally two solutions in the PK subproblems 1 and 2, and the sum value of the two solutions is π or -π. The correct solution can be obtained by setting the constraint conditions. The PK subproblem 3 yields two solutions, and the solution with the smaller absolute displacement is correct.

3. Error and sensitivity analysis

3.1. Error modeling of the PUS chain

A closed-loop vector method is used for the error analysis of the 5PUS-RPUR parallel robot. Considering the manufacturing and assembly errors, the error mapping model of the PUS chain is analyzed. On the basis of Fig. 3(b), the geometric errors in the PUS chain are described in Fig. 4.

From the analysis of the inverse kinematics, the pose mapping relationship between the moving platform and the actuator joints only requires the initial and final pose of the moving platform, and the position vector of the U center point A_i and the S center point B_i. The main factors affecting the position vector of point A include the module position deviation $\Delta\psi_{1i}$, the side plate angle deviation $\Delta\lambda_i$, the actuator zero-point error $\Delta\theta_i$, and the manufacturing error of the base length ΔD_i. The position error of the vector O_iB_i is affected by the assembly error $\Delta\psi_{2i}$ of the spherical pair and the manufacturing error Δd_i of the bearing. Considering the above conversion errors, the forward kinematics of the PUS chain can be expressed as

$$\Delta \boldsymbol{g}(\theta) = \prod_{j=1}^{6} \exp\left(\Delta\hat{\xi}_{i,j}, \Delta\theta_{i,j}\right) \cdot \Delta \boldsymbol{g}(0), \ i = 1 \sim 5 \tag{22}$$

$$\begin{cases} \Delta\hat{\xi}_{i,1} = [000, \Delta s_{i,1}]^T, \Delta s_{i,1} = \boldsymbol{R}_{i,1}[001]^T, \boldsymbol{R}_{i,1} = \boldsymbol{Rz}\left(2\left(i-1\right)\pi/5\right)\boldsymbol{Ry}(\lambda+\Delta\lambda-\pi/2) \\ \Delta\hat{\xi}_{i,2} = \left[\Delta s_{i,2}{}^0\boldsymbol{P}_{Ai} \times s_{i,2}\right]^T, \Delta s_{i,2} = \boldsymbol{R}_{i,2}\boldsymbol{e}_y, \boldsymbol{R}_{i,2} = \boldsymbol{Rz}\left(2\left(i-1\right)\pi/5\right)\boldsymbol{Ry}(-\varphi_i)\boldsymbol{Ry}(\Delta\lambda) \\ \Delta\hat{\xi}_{i,3} = \left[\Delta s_{i,3}{}^0\boldsymbol{P}_{Ai} \times s_{i,3}\right]^T, \Delta s_{i,3} = \boldsymbol{R}_{i,3}\boldsymbol{e}_x, \boldsymbol{R}_{i,3} = \boldsymbol{R}_{i,2}\boldsymbol{Ry}(\Delta\psi_{U11}) \\ \Delta\hat{\xi}_{i,4} = \left[\Delta s_{i,4}{}^0\boldsymbol{P}_{Bi} \times \Delta s_{i,4}\right]^T, \Delta s_{i,4} = \boldsymbol{R}_{i,4}\boldsymbol{e}_x, \boldsymbol{R}_{i,4} = \boldsymbol{R}_{i,3}\boldsymbol{Rx}(\Delta\psi_{U12}) \\ \Delta\hat{\xi}_{i,5} = \left[\Delta s_{i,5}{}^0\boldsymbol{P}_{Bi} \times \Delta s_{i,5}\right]^T, \Delta s_{i,5} = \boldsymbol{R}_{i,5}\boldsymbol{e}_y, \boldsymbol{R}_{i,5} = \boldsymbol{R}_{i,4}\boldsymbol{Ry}(\Delta S_{11}) \\ \Delta\hat{\xi}_{i,6} = \left[\Delta s_{i,6}{}^0\boldsymbol{P}_{Bi} \times \Delta s_{i,6}\right]^T, \Delta s_{i,6} = \boldsymbol{R}_{i,6}\boldsymbol{e}_z, \boldsymbol{R}_{i,6} = \boldsymbol{R}_{i,5}\boldsymbol{Rx}(\Delta S_{12}) \end{cases} \tag{22a}$$
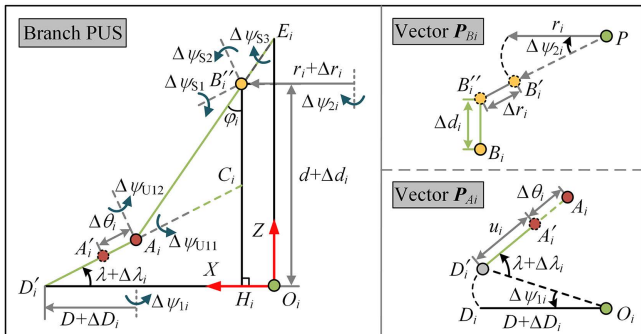
Fig 4. Structure diagram of branched PUS with errors.

$$\begin{cases} {}^{0}\boldsymbol{P}_{Ai} = \boldsymbol{O}_i\boldsymbol{D}'_i + \boldsymbol{D}'_i\boldsymbol{A}_i, {}^{0}\boldsymbol{P}_{Bi} = \boldsymbol{O}_i\boldsymbol{B}'_i + \boldsymbol{B}'_i\boldsymbol{B}_i \\ \boldsymbol{O}_i\boldsymbol{D}'_i = \boldsymbol{R}z\left(2\left(i-1\right)\pi/5 + \Delta\psi_{1i}\right)\boldsymbol{D}_i, \boldsymbol{D}_i = [D + \Delta D_i\ 0\ 0]^{\mathsf{T}} \\ \boldsymbol{D}'_i\boldsymbol{A}_i = \left(u_i + \Delta\theta_i\right)\left[\boldsymbol{R}z\left(2\left(i-1\right)\pi/5 + \Delta\psi_{1i}\right)\left(\boldsymbol{R}y\left(-\lambda - \Delta\lambda_i\right)\right)\boldsymbol{e}_z\right] \\ \boldsymbol{O}_i\boldsymbol{B}'_i = \Delta\boldsymbol{R}^{N}\boldsymbol{B}_i + \Delta\boldsymbol{P}, \Delta\boldsymbol{R} = \boldsymbol{R}_x(\Delta\alpha)\boldsymbol{R}_y(\Delta\beta), {}^{N}\boldsymbol{B}_i = [0\ 0\ \Delta d_i]^{\mathsf{T}} \\ \boldsymbol{B}'_i\boldsymbol{B}_i = \boldsymbol{R}z\left(2\left(i-1\right)\pi/5 + \Delta\psi_{2i}\right)\left(\boldsymbol{P}\boldsymbol{B}'_i + \boldsymbol{B}''_i\boldsymbol{B}_i\right) \\ \boldsymbol{P}\boldsymbol{B}'_i = [r_i\ 0\ 0]^{\mathsf{T}}, \boldsymbol{B}''_i\boldsymbol{B}_i = [\Delta r_i\ 0\ \Delta d_i]^{\mathsf{T}}, \Delta\boldsymbol{P} = [\Delta x\ \Delta y\ \Delta z]^{\mathsf{T}} \end{cases} \tag{22b}$$

where $\Delta\hat{\boldsymbol{\xi}}_{i,j}$ denotes the screw axis of the *j*-th joint in the *i*-th PUS limb, considering geometric errors. $\Delta\hat{\theta}_{i,j}$ represents the actual joint displacement, inclusive of geometric errors. $\boldsymbol{e}_x$, $\boldsymbol{e}_y$ and $\boldsymbol{e}_z$ are the unit vectors along the *X*, *Y*, and *Z* axes of the fixed coordinate frame. ${}^{0}\boldsymbol{P}_{Ai}$ and ${}^{0}\boldsymbol{P}_{Bi}$ denote the position vectors of the center points of the U and S at the initial pose. $\Delta\boldsymbol{P}$ and $\Delta\boldsymbol{R}$ represent the initial position and posture error of the moving platform, respectively. φ_i is the nominal angle between the constant-length link A_iB_i and the Z-axis of the fixed frame. r_i and d are the distance of point B_i from the origin of the moving coordinates and the distance of point B from the *XOY* plane. The parameters with manufacturing error include Δr_i, ΔD_i and Δd_i, and the parameters with assembly error include $\Delta\psi_{1i}$, $\Delta\psi_{2i}$ and $\Delta\lambda_i$. By replacing the vector points $\boldsymbol{P}_{Ai}$ and $\boldsymbol{P}_{Bi}$ in the inverse kinematics of the PUS chain with the vectors ${}^{0}\boldsymbol{P}_{Ai}$ and ${}^{0}\boldsymbol{P}_{Bi}$.

3.2. Error modeling of the RPUR chain

The geometric errors in the RPUR chain are described in [Fig 5](), including the assembly pose error of R1, the initial position error of the electric cylinder, the angular error of U2, the assembly pose error of R2, and the initial pose error of the moving platform. The relationship between these geometric source errors and the pose of the moving platform is established using forward kinematics and can be formulated as

$$\Delta\boldsymbol{g}(\theta) = \prod_{j=1}^{5}\exp\left(\Delta\hat{\boldsymbol{\xi}}_{i,j}, \Delta\theta_{i,j}\right)\cdot\Delta\boldsymbol{g}\left(0\right), i = 6 \tag{23}$$
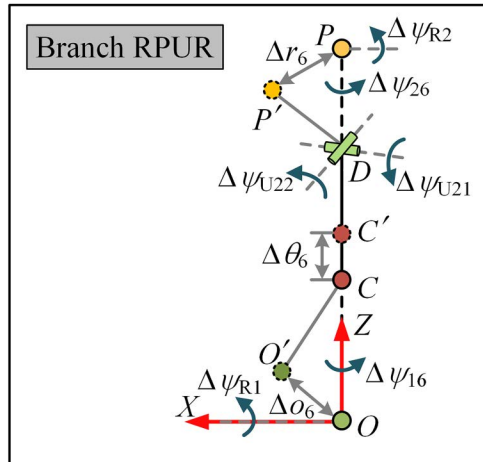
Fig 5. Structure diagram of branched RPUR with errors.

$$
\begin{cases}
\Delta\hat{\xi}_{6,1} = [\Delta s_{i,1} \; {}^0\boldsymbol{P}_o \times \Delta s_{i,1}]^T, \Delta s_{i,1} = \boldsymbol{R}_{6,1}[100]^T, \boldsymbol{R}_{6,1} = \boldsymbol{Rz}(\Delta\psi_{16}) \\
\Delta\hat{\xi}_{6,2} = [000\Delta s_{6,2}]^T, \Delta s_{6,2} = \boldsymbol{R}_{6,2}[001]^T, \boldsymbol{R}_{6,2} = \boldsymbol{R}_{6,1}\boldsymbol{Rx}(\Delta\psi_{R1}) \\
\Delta\hat{\xi}_{6,3} = [\Delta s_{6,3}{}^0\boldsymbol{P}_D \times s_{6,3}]^T, \Delta s_{6,3} = \boldsymbol{R}_{6,3}[100]^T, \boldsymbol{R}_{6,3} = \boldsymbol{R}_{6,2}\boldsymbol{Ry}(\Delta\psi_{U22}) \\
\Delta\hat{\xi}_{6,4} = [\Delta s_{6,4}{}^0\boldsymbol{P}_D \times s_{6,4}]^T, \Delta s_{6,4} = \boldsymbol{R}_{6,4}[0\;10]^T, \boldsymbol{R}_{6,4} = \boldsymbol{R}_{6,3}\boldsymbol{Rx}(\Delta\psi_{U21}) \\
\Delta\hat{\xi}_{6,5} = [\Delta s_{6,5}{}^0\boldsymbol{P}_{P'} \times s_{6,5}]^T, \Delta s_{6,5} = \boldsymbol{R}_{6,5}[010]^T, \boldsymbol{R}_{6,5} = \boldsymbol{R}_{6,5}\boldsymbol{Rz}(\Delta\psi_{26})
\end{cases}
\tag{23a}
$$

$$
\begin{cases}
{}^0\boldsymbol{P}_D = {}^0\boldsymbol{P}_{O'} + \boldsymbol{O'C} + \boldsymbol{CD}, {}^0\boldsymbol{P}_{P'} = \boldsymbol{Rx}(\Delta\psi_{R2})\,\boldsymbol{Rz}(\Delta\psi_{26})\,[\Delta r_6\;0\;0]^T \\
{}^0\boldsymbol{P}_{O'} = \boldsymbol{Rz}(\Delta\psi_{16})\,[^\Delta, \boldsymbol{O'C} = \boldsymbol{Rx}(\Delta\psi_{r1})\,[0\;0\;l_c]^T, \boldsymbol{CD} = [0\;0\;l_d + \Delta\theta_6]^T
\end{cases}
\tag{23b}
$$

where ${}^0\boldsymbol{P}_{O'}$, ${}^0\boldsymbol{P}_D$ and ${}^0\boldsymbol{P}_{P'}$ denote the position vectors of the center points of the O', D and P' at the initial pose. l_c is the center distance from the electric cylinder to U2, and l_d is the center distance from push rod to the origin. $\Delta\theta_6$ represents the zero-position error of the electric cylinder, and $\Delta\psi_{r1}$ represents the initial deviation of R1.

3.3. Sensitivity analysis

As stated above, there are 69 error sources affecting the moving platform pose accuracy of the parallel robot. The individual identification of each source is complex, tedious, and computationally expensive. Therefore, a geometric error sensitivity model is established to screen out errors that have a minor impact on the moving platform pose. The mapping between the geometric errors and the moving platform's pose can be obtained from Eqs. (22) and (23). Taking the degree of freedom of the PUS chain in the x-direction as an example, the sensitivity index is established as follows

$$
\eta_{xi} = \frac{\partial x}{\partial q_{pi}}
\tag{24}
$$

where q_{pi} denotes the vector of geometric error sources affecting the position x, namely q_{pi}: {$\Delta\psi_{1i}$, $\Delta\psi_{2i}$, $\Delta\lambda_i$, ΔD_i, Δr_i, Δd_i, $\Delta\theta_i$}. Additionally, the other error vectors include $q_{\omega i}$: {$\Delta\psi_{1i}$, $\Delta\psi_{2i}$, $\Delta\lambda_i$, $\Delta^1\psi_{U11}$, $\Delta^1\psi_{U12}$, $\Delta\psi_{S11}$, $\Delta\psi_{S12}$, $\Delta\psi_{S13}$}, q_{p6}: {$\Delta\psi_{R1}$, $\Delta\psi_{16}$, Δo_6, $\Delta\theta_6$, $\Delta\psi_{R2}$, $\Delta\psi_{16}$, Δr_6}, and $q_{\omega 6}$: {$\Delta\psi_{R1}$, $\Delta\psi_{16}$, $\Delta\psi_{R2}$, $\Delta\psi_{26}$, $\Delta\psi_{U21}$, $\Delta\psi_{U22}$}.

In order to visually analyze the workspace, the Tilt-and-Torsion (T&T) angle containing azimuth ϕ_P, tilt θ_P and torsion ψ_P is used to describe the posture change of the parallel robot [28]. The rotation matrix of the T&T angle can be expressed as

$$
{}^{TT}\boldsymbol{R}(\phi_P, \theta_P, 0) = \boldsymbol{R}_z(\phi_P)\,\boldsymbol{R}_y(\theta_P)\,\boldsymbol{R}_z(-\phi_P)\,\boldsymbol{R}_z(0)
\tag{25}
$$

Due to the degree of freedom property of the 5PUS-RPUR parallel robot, the Euler angle γ of rotation of the moving platform around the z-axis is equal to 0. The Euler angles are converted into the T&T angle form, which can be expressed as

$$
\begin{cases}
\alpha = \operatorname{asin}(-\sin\phi_P \sin\theta_P) \\
\beta = \operatorname{asin}(\cos\phi_P \sin\theta_P)
\end{cases}
\tag{26}
$$

The workspace of the 5PUS-RPUR parallel robot is limited by the range of the actuators, the mechanical limit of passive joints and the interference between links. The mathematical expression of the workspace is

$$
W = \left\{ (x, y, z, \phi_P, \theta_P) \in \boldsymbol{R}^5 \,\middle|\, \boldsymbol{f}(x, y, z, \phi_P, \theta_P) \leq \boldsymbol{0} \right\}
\tag{27}
$$

where $\boldsymbol{f}(\cdot)$ denotes the constraints, which include rod length, corner and link interference constraints. x, y, z and ϕ_P, θ_P are the position and posture parameters of the moving platform respectively. For the 5PUS-RPUR parallel robot, the x limit

range is determined by the length of the fixed-length rod 2, the y limit range is the sum of the parameter d and the maximum displacement of the actuator, and the z limit range is the maximum displacement of the actuator. While the azimuth angle ϕ_P is within $[0, 2\pi]$ and the tilt angle θ_P is within $[0, \pi/2]$. Then, the above pose parameters are evenly divided, and the divided parameters are combined and substituted into the inverse kinematics of the PUS and RPUR chains to obtain the poses of the parallel robot's components. After that, it is judged whether the poses satisfy the constraints; all valid poses satisfying the constraints constitute the reachable workspace of the parallel robot.

(1) Rod length constraints: $\theta_{min} \leq \theta_i \leq \theta_{max}$ ($i = 1 \sim 5$), θ_{min} and θ_{max} indicate the minimum and maximum displacements of the actuator joint.

(2) Corner constraints: $\theta_{Ui} = \arccos[\hat{\boldsymbol{L}}_i \cdot (\boldsymbol{s}_{i,2} \times \boldsymbol{s}_{i,3})] \leq \theta_{U\max}$,

$\theta_{Si} = \arccos(\hat{\boldsymbol{L}}_i \cdot \boldsymbol{s}_{i,6}) \leq \theta_{S\max}$, $\theta_{U\max}$ and $\theta_{S\max}$ indicate the maximum rotation angle of the U and S pair.

(3) Link interference constraints: $d_R \geq d_{sa}$, $D_{P6} \geq D_1 + D_2$, d_{sa} is the interference distance between the fixed-length rod 2 and the moving platform, which can be limited with the rotation angle of the R pair in the RPUR chain connected to the moving platform. Without loss of generality, the actuator joints of the RPUR and PUS chains are equated to spheres with diameters D_1 and D_2, respectively.

As shown in Fig. 6, the reachable workspace of the 5PUS-RPUR parallel robot is analyzed by the search method. First, the range of pose parameters x, y, z and ϕ_P, θ_P are determined according to the structural characteristics, and the
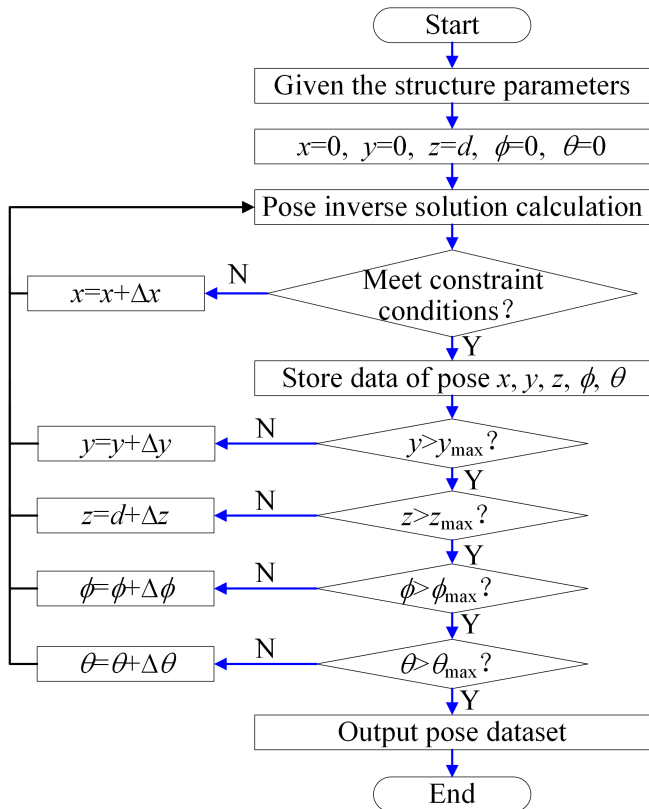
Fig 6. Flow diagram of the reachable workspace.

structure size of the parallel robot is given in Table 1. Next, the step size of pose parameters is set to $\Delta x = \Delta y = \Delta z = 0.01$m and $\Delta\phi_P = \Delta\theta_P = \pi/60$ rad. Substitute the initial values of the moving platform's pose parameters into the inverse kinematics of the parallel robot to obtain the poses of each component, and then iteratively check whether the current pose parameters of the moving platform satisfy the rod length, corner, and link interference constraints. If the constraints are satisfied, store the current poses; otherwise, discard the poses. Finally, the set of all poses satisfying the constraints is output, which represents the reachable workspace of the parallel robot's moving platform.

Following the steps in Fig 6 the parallel robot pose reachable workspace is obtained as shown in Fig 7. From the side view, the position workspace of the reference point is trapezoidal distribution, which is determined by the structure of the parallel robot. On the other hand, the posture workspace is basically enveloped in an entire circle, which can achieve flexible rotation within a limited range.

Given the strong coupling and nonlinear characteristics inherent among the source errors in Eq. (24), deriving an independent analytical relationship between each error and the moving platform's pose is exceedingly difficult. Therefore, a numerical method is employed to solve for the partial derivatives [29]. The mean sensitivity of each error source is calculated at different pose points based on the structural parameters mentioned above. The resulting histograms of the mean sensitivity for position and posture errors are shown in Figs 8 and 9, respectively. It can be observed that the robot's moving platform pose is highly sensitive to angular variations within the geometric errors. The error sources with a minor impact on the moving platform's position error, namely ΔD_i, $\Delta\theta_i$, Δo_6, and $\Delta\theta_6$, are screened out to simplify the complexity and improve the efficiency of parameter identification.

**Table 1. Size parameters of the 5PUS-RPUR parallel robot.**

| Parameter	Symbol	Value (unit)
Center distance from 1# S pair to movable platform	r_1	200 mm
Center distance from 2# S pair to movable platform	r_2	213.13 mm
Center distance from 3# S pair to movable platform	r_3	225.60 mm
Center distance from 4# S pair to movable platform	r_4	237.47 mm
Center distance from 5# S pair to movable platform	r_5	248.78 mm
Center distance from the electric cylinder to the universal joint 2	l_c	514 mm
Center distance from push rod to origin	l_d	113 mm
Distance from the intersection of the side plate plane and the X-axis to the origin	D	1000 mm
Distance from point B to XOY plane	d	760 mm
Length of fixed-length rod 1	l_1	600 mm
Length of fixed-length rod 2	l_2	132 mm
Side plate angle	λ	30°
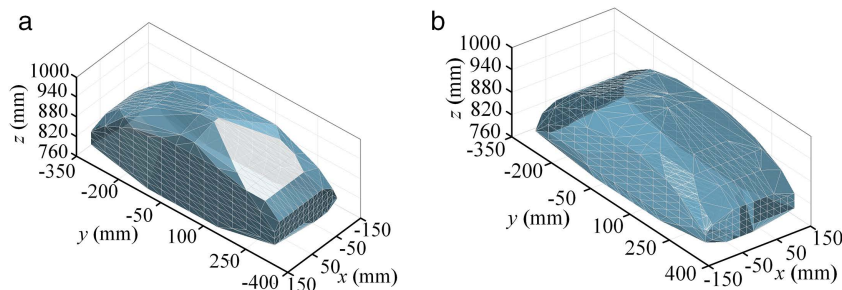
Fig 7. Reachable pose workspace of the 5PUS-RPUR parallel robot. (a) Position workspace (left view). **(b)** Position workspace (right view).
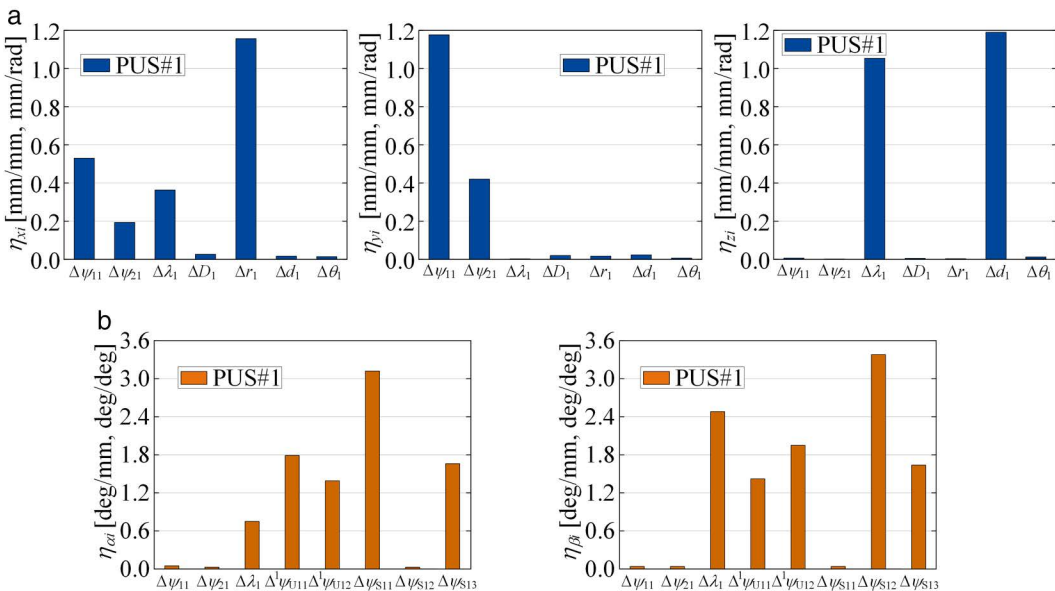
Fig 8. Mean of sensitivity indices of PUS chain throughout the reachable workspace. (a) Mean of position sensitivity indices of PUS chain. **(b)** Mean of posture sensitivity indices of PUS chain.

https://doi.org/10.1371/journal.pone.0330675.g008
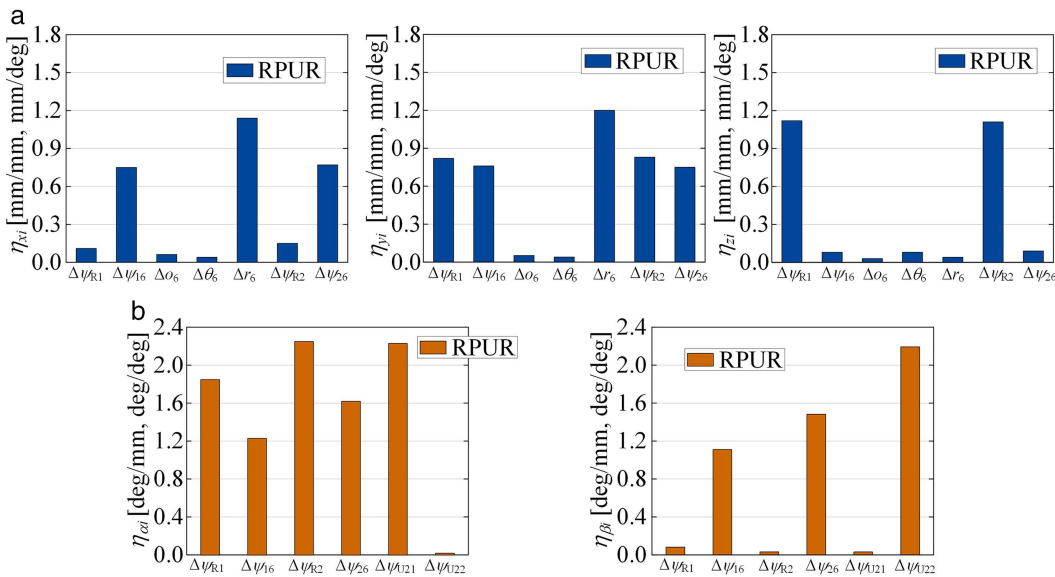
Fig 9. Mean of sensitivity indices of RPUR chain throughout the reachable workspace. (a) Mean of position sensitivity indices of PRUR chain. **(b)** Mean of posture sensitivity indices of PRUR chain.

https://doi.org/10.1371/journal.pone.0330675.g009

4. Kinematic calibration

To ensure the effective identification of geometric source errors, the selection of measured points is crucial. The measured points should go through all controllable degrees of freedom. Moreover, it is believed that measuring enough poses is beneficial to increase the identification robustness [30]. However, in practical applications, a compromise must be struck

between identification robustness and calibration efficiency. Research indicates that the number of identification equations should be at least twice the number of parameters to be identified [19]. Following a sensitivity analysis, 57 parameters have been identified for estimation, dictating a requirement for no fewer than 114 measurement poses. In light of this, 121 uniform measured points are selected within the prescribed workspace using a farthest point sampling algorithm [31]. This set includes 11 position points, with 11 different posture points selected at each of these fixed positions. The specific distribution is illustrated in Figs 10 and 11.

Fig 11 shows the distribution of measured posture points when the moving platform's reference point is fixed at P_3 = [−11.6, −115.4, 860] mm. This distribution is also generated using the farthest point sampling algorithm.

To validate the kinematic calibration process of the 5PUS-RPUR parallel robot, the kinematic calibration experiment is carried out. The 5PUS-RPUR parallel robot system is built as shown in Fig 12, including a host computer, GTS motion control card, IMU sensor, servo motor with encoder and parallel mechanism body.

In the kinematic calibration experiment, the theoretical displacement of each actuator is obtained by applying theoretical pose measured points of the moving platform to the inverse kinematics. The motion command of the theoretical displacement is input in the host computer, and the pose variation of the moving platform is measured by IMU. Considering the manufacturing and assembly errors and the initial pose deviation of the moving platform, the IMU measured data is substituted into the error mapping model. It should be noted that the IMU cannot measure absolute poses. The joint displacement calculated by the first collected data is used as the reference, and the joint displacement obtained by other pose data minus the reference is used as the available data. Furthermore, exclusively considering the discrepancy in actuator displacement, derived from encoder and IMU data, while neglecting the coupling effects between kinematic chains, would inevitably introduce coupling errors and degrade the identification accuracy. Therefore, a comprehensive objective function is established by integrating the actuator displacement deviations with the pose error of the moving platform. This can be expressed as:

$$
\begin{cases}
\min f(\boldsymbol{X}) = (1 - \varpi_1 - \varpi_2) \sum_{i=1}^{6} \left\| \Delta\theta_i^e - \Delta\theta_i^{\mathsf{IMU}} \right\| + \sum_{i=1}^{6} (\varpi_1 \Delta E_{Pi} + \varpi_2 \Delta E_{Ri}) \; (i = 1 \sim 6) \\
s.t. \;\; \boldsymbol{X} \in R, R \subseteq U, \;\; l_1 - \Delta l_1 \leq \| \boldsymbol{P}_{Ai} - \boldsymbol{P}_{Bi} \| \leq l_1 + \Delta l_1, \;\; l_2 - \Delta l_2 \leq \| \boldsymbol{P}_D - \boldsymbol{P}_{P'} \| \leq l_2 + \Delta l_2
\end{cases}
$$

(28)
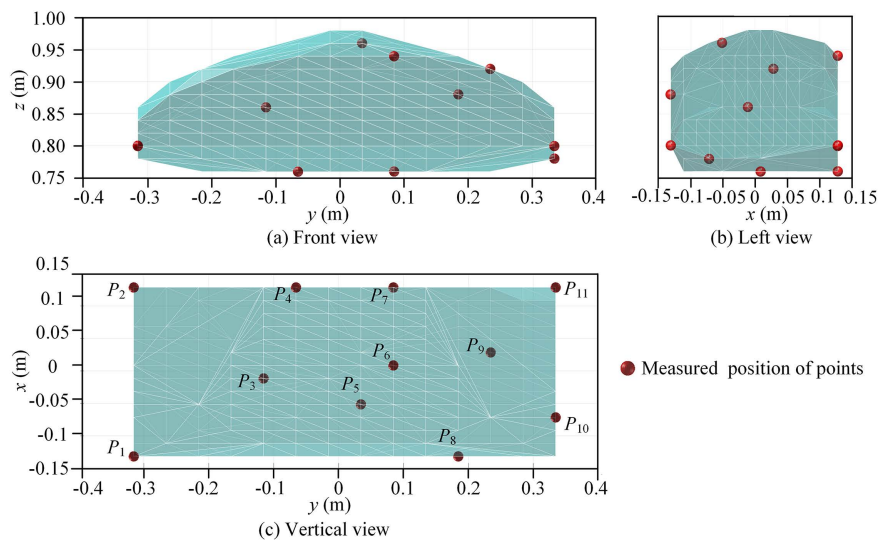
**Fig 10. Distribution of measured points in the position workspace.**
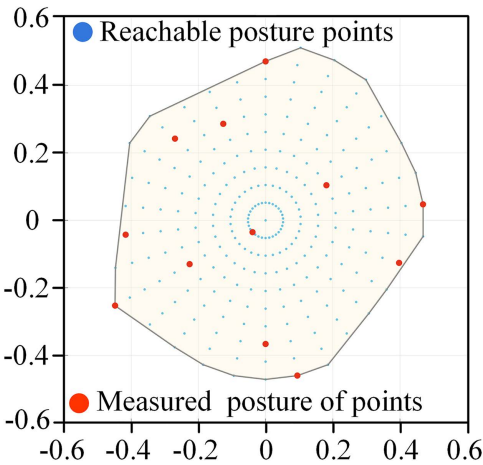
Fig 11. Distribution of posture measured points at the fixed position.
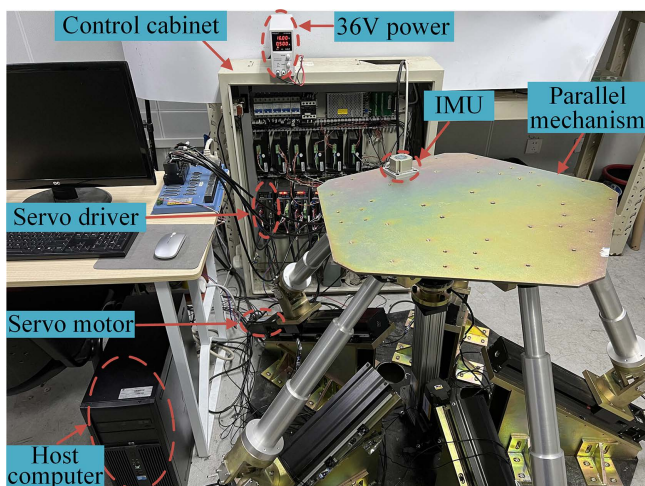
Fig 12. 5PUS-RPUR parallel robot system.

where ΔE_{pi} and ΔE_{ri} represent the Euclidean norms of the position and posture errors of the moving platform, respectively, as derived from the forward kinematics of each chain. The terms ϖ_1 and ϖ_2 are weighting factors that balance the contribution of the position and posture errors. It is important to note that to address the issue of dimensional inconsistency, all three sub-terms within $f(\boldsymbol{X})$ have been normalized using min-max scaling [32]. $\boldsymbol{X}$ represents variables such as manufacturing error and assembly error, initial pose deviation and pose offset of moving platform. θ_i^e and θ_i^{IMU} indicate the actuator displacement measured by the encoder and obtained by substituting IMU data into the error mapping model. i denotes the branch number. U represents the basic space of decision variables, and R is a subset of U. The solution X satisfying the constraint condition is called the feasible solution, and the set R represents the set of feasible solutions. l_1 and l_2 denote the length of the fixed-length rod 1 and 2. Δl_1 and Δl_2 is the manufacturing error of the fixed-length rod 1 and 2 to be measured using a high-precision instrument. In the process of establishing the error model, only the vector position of the

two ends of the fixed-length rod is described from the base and the moving platform, and the rod length error needs to be added to ensure the rationality of the model.

Genetic algorithm has the advantages of good generalization, strong robustness and global optimality in dealing with nonlinear constraints [33]. Due to it being time-consuming to deal with nonlinear constraints, Eq. (28) can be transformed into an unconstrained problem through a penalty function method.

$$f_P(\boldsymbol{X}) = f(\boldsymbol{X}) + \sum_{i=1}^{5} G \left\{ \max \left[\|\boldsymbol{P}_{Ai} - \boldsymbol{P}_{Bi}\| - (l_1 + \Delta l_1), 0 \right] + \max \left[(l_1 - \Delta l_1) - \|\boldsymbol{P}_{Ai} - \boldsymbol{P}_{Bi}\|, 0 \right] \right\}$$
$$+ H \left\{ \max \left[\|\boldsymbol{P}_D - \boldsymbol{P}_{P'}\| - (l_2 + \Delta l_2), 0 \right] + \max \left[(l_2 - \Delta l_2) - \|\boldsymbol{P}_D - \boldsymbol{P}_{P'}\|, 0 \right] \right\}$$

(29)

where G and H are penalty factors, which are typically set to large positive values. According to the evolutionary mechanism of the genetic algorithm, the population will autonomously avoid solutions that do not satisfy the constraints during the evolutionary process. The optimal error parameters can be identified using genetic algorithms, and the errors of manufacturing, assembly and actuator initial positions can be compensated to improve the pose accuracy of the parallel robot.

The pose data of the moving platform and the displacement of the actuator measured by IMU and encoder are substituted into Eq. (30). The initialization parameters of genetic algorithm are as follows: population = 200, iteration number = 100, crossover probability = 0.8, mutation probability = 0.05. The optimization results are shown in Table 2 and Table 3.

After performing the kinematic calibration, the identified parameters are embedded into the control model, replacing the nominal ones. To evaluate the kinematic calibration experiment, the pose accuracy is analyzed using the pose points of another 36 test poses points before and after kinematic calibration. The pose points consist of 9 uniformly selected position points, with 4 posture points chosen at each position, corresponding to the maximum and minimum posture values. The corresponding data are presented in Table 4. The data processing for encoders and IMU sensors is embedded in the proprietary software, where the manufacturers have performed filtering, outlier removal, and smoothing of the measurement data.

The error curves before calibration (BC) and after identification (AC) are obtained at the aforementioned measured points as shown in Fig 13.

It can be seen from Fig 13 that after the error compensation of manufacturing, assembly and actuator, the accuracy error is reduced from 3.41 mm, 4.18 mm, 2.97 mm, 1.11°and 0.84° to 0.53 mm, 0.88 mm, 0.42 mm, 0.43° and 0.34° in

Table 2. Optimization results of manufacturing and assembly errors in the PUS chain.

CN	$\Delta\psi_1 i$	$\Delta\psi_2 i$	$\Delta\lambda i$	$\Delta r i$	$\Delta d i$	$\Delta\psi U i_1$	$\Delta\psi U i_2$	$\Delta\psi S i_1$	$\Delta\psi S i_2$	$\Delta\psi S i_3$
PUS#1	−0.08	0.14	0.076	−0.98	−1.11	−0.04	0.04	0.01	0.04	0.06
PUS#2	−0.06	0.09	0.081	−0.89	−1.04	0.03	0.07	−0.02	0.01	−0.02
PUS#3	0.09	−0.21	−0.071	0.88	0.94	−0.06	−0.06	0.03	−0.03	0.01
PUS#4	0.12	−0.24	0.049	−1.02	−0.96	0.06	0.07	−0.01	−0.03	−0.03
PUS#5	−0.11	0.18	0.062	1.06	0.87	0.05	−0.04	0.02	0.02	0.04

Note: Angle unit: °, length unit: mm, Chain number (CN).

https://doi.org/10.1371/journal.pone.0330675.t002

Table 3. Optimization results of manufacturing and assembly errors in the RPUR chain.

Chain	$\Delta\psi R_1$	$\Delta\psi_{16}$	Δo_6	$\Delta\psi R_2$	$\Delta\psi_{26}$	$\Delta\psi U_{21}$	$\Delta\psi U_{22}$
RPUR	0.08	−0.06	0.16	−0.07	0.03	0.08	−0.06

Note: Angle unit: °, length unit: mm, Chain number (CN).

https://doi.org/10.1371/journal.pone.0330675.t003

Table 4. Dataset of measurement poses and actuator displacements.

Measured point	Δx	Δy	Δz	Δα	Δβ	θ_1^e	θ_2^e	θ_3^e	θ_4^e	θ_5^e
1	−131.18	335.3	760.33	−20.08	−21.50	233.96	−69.80	−221.88	−15.60	259.14
2	−131.20	335.3	760.36	−20.10	24.53	50.24	−122.26	−19.08	259.62	170.34
3	−131.14	335.1	760.40	21.98	−21.53	207.99	111.13	−143.52	−41.28	102.32
4	−131.12	335.1	760.36	21.88	24.53	76.52	15.74	123.86	85.40	74.24
5	−131.15	10.29	920.38	−20.97	−22.33	376.63	167.28	−6.60	82.35	421.46
6	−131.16	10.27	920.30	−20.93	25.39	153.53	104.11	247.87	534.20	281.99
7	−131.10	10.35	920.34	22.77	−22.28	373.81	382.05	86.79	−7.73	160.47
8	−131.07	10.36	920.37	22.69	25.39	155.84	269.92	494.51	250.83	91.03
9	−131.14	−314.64	760.42	−20.07	−21.66	208.30	108.93	−46.27	−149.05	140.26
10	−131.18	−314.62	760.31	−20.04	24.43	70.53	81.62	82.30	137.15	23.93
11	−131.18	−314.65	760.31	21.99	−21.60	230.52	242.87	−15.72	−224.92	−76.62
12	−131.15	−314.64	760.28	21.96	24.54	48.15	167.61	244.79	−18.86	−134.30
13	−1.14	−314.60	870.38	−22.40	−22.89	276.21	159.78	86.61	55.63	319.89
14	−1.12	−314.54	870.40	−22.27	26.99	62.52	119.61	243.10	398.26	142.93
15	−1.09	−314.62	870.40	23.73	−22.87	310.95	340.89	133.42	−53.23	−6.71
16	−1.11	−314.66	870.35	23.83	27.03	33.78	243.20	419.50	216.97	−88.72
17	−1.18	10.27	980.34	−17.67	−15.99	392.17	208.47	128.16	223.30	477.23
18	−1.19	10.27	980.37	−17.70	18.44	150.62	145.32	335.57	531.07	342.01
19	−1.12	10.12	980.40	16.57	−16.03	392.56	410.95	216.60	128.48	219.17
20	−1.09	10.11	980.37	16.48	18.43	150.40	306.45	498.95	351.80	142.71
21	−1.13	335.21	870.38	−22.17	−22.83	316.70	−0.99	−48.13	132.48	369.04
22	−1.16	335.28	870.29	−22.13	26.90	35.47	−74.39	215.56	435.53	250.94
23	−1.08	335.32	870.34	23.67	−22.77	276.35	259.43	61.16	89.33	154.93
24	−1.07	335.38	870.35	23.60	26.90	69.03	123.24	377.20	246.61	111.14
25	128.88	335.37	760.42	−20.27	−21.67	107.27	−145.35	−42.27	104.19	238.27
26	128.79	335.39	760.30	−20.23	24.63	−141.52	−200.57	136.70	313.90	135.60
27	128.82	335.34	760.29	21.99	−21.60	74.16	51.39	30.76	83.40	61.84
28	128.87	335.40	760.26	21.96	24.73	−113.15	−55.89	237.96	186.35	29.75
29	128.88	10.42	920.36	−21.20	−22.40	328.31	123.09	117.42	191.90	425.88
30	128.88	10.45	920.42	−21.06	25.50	−2.14	54.45	319.85	475.62	252.67
31	128.91	10.35	920.40	22.82	−22.36	324.25	372.08	196.54	114.75	118.27
32	128.93	10.32	920.35	22.93	25.54	0.68	237.55	461.95	320.03	41.48
33	128.82	−314.78	760.33	−19.87	−21.50	73.51	67.82	80.49	23.94	82.74
34	128.80	−314.74	760.38	−19.89	24.33	−119.69	36.82	184.44	244.00	−46.54
35	128.89	−314.87	760.41	22.17	−21.54	101.04	217.64	105.90	−47.03	−151.54
36	128.79	−315.10	760.23	22.00	24.27	−142.88	131.65	302.29	133.03	−211.36

Note: Angle unit: °, length unit: mm.

direction of the position *x*, *y*, *z*, angle *α* and *β*. The positioning accuracy of the five-degree-of-freedom direction of the parallel robot is improved by 84.4%, 78.9%, 85.8%, 61.2%, and 59.1%, respectively. The effectiveness of the calibration algorithm is verified through the experimental results.

A paired t-test [34] is employed to verify the statistical significance of the pose errors. Table 5 lists the p-values from the t-test for the errors in the five DOF before and after identification. The p-values from the paired t-test are all less than 0.05.
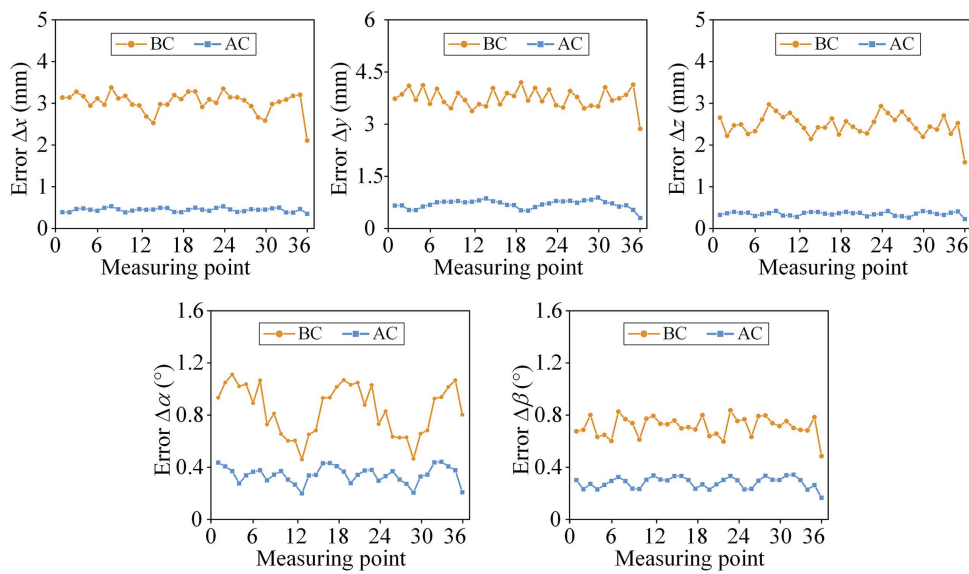
Fig 13. Errors of positions and postures before and after calibration compensation.

**Table 5. p-values of the paired t-tests in the five DOF directions.**

Freedom direction	t	p
x	63.2492123769993	5.56698869303580e-38
y	60.3073254364646	2.90529360520355e-37
z	49.6607674371379	2.41149451739672e-34
α	18.4220716298725	6.82735670364796e-20
β	41.3926351741914	1.27385246363205e-31

It is concluded from Table 5 that considering the manufacturing and assembly errors of the components, the pose accuracy after kinematic calibration is acceptable.

To further validate the superiority of the proposed algorithm, a comparative study is conducted by performing kinematic calibration using artificial neural networks (ANN) [17], Levenberg-Marquardt algorithm (LMA) [16], and gradient-based optimizer (GBO) [35]. The identification parameters rather than the original parameters will be embedded into the control model. The mean and standard deviation of the errors are presented in Fig 14, where the scalar values for position and orientation errors are obtained via their Euclidean norms. It can be observed that the GA yields the lowest mean and standard deviation for both position and orientation errors, particularly in terms of position error. Although this superior accuracy is achieved at the expense of a higher computational cost, this is not a significant drawback, as offline calibration procedures are typically not subject to stringent time constraints.

The proposed self-calibration method is applicable to other parallel robots. The robot's kinematic model is likewise established within the mathematical framework of screw theory, and an error model is constructed by means of the forward kinematics. By mounting sensors on the moving platform and the actuators, motion data from the actuated joints and the moving platform can be acquired. These data are then used in conjunction with a heuristic algorithm to identify the error parameters.
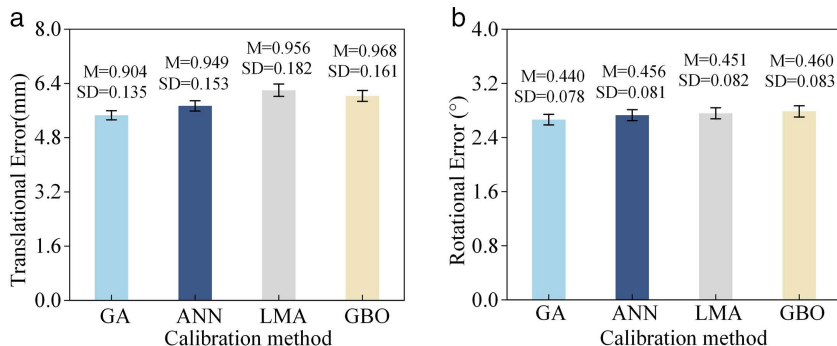
Fig 14. Pose errors of 5PUS-RPUR robot with different algorithms. (a) Position errors. **(B)** Posture errors.

5. Conclusions

In order to improve the pose accuracy of the 5PUS-RPUR parallel robot, a method of kinematic error analysis and identification of the parallel robot is proposed. The main conclusions are as follows.

1) Combined with the screw theory, PK subproblems and elimination method, the inverse displacement of the series chain is analyzed to obtain the analytical solution of the inverse kinematics of the parallel robot.

2) The farthest point sampling algorithm is utilized to select measurement points uniformly throughout the robot's workspace. This strategy ensures a comprehensive coverage of global errors, which is beneficial for improving the precision of the identification process.

3) By constructing an objective function that incorporates both the actuator displacement errors from each chain with the overall pose error of the moving platform, the coupling effects between chain parameters can be indirectly eliminated. This approach facilitates a globally optimal error identification result, thereby enhancing the pose accuracy of the parallel manipulator in all directions.

Future work will address errors that arise under dynamic loading, taking into account non-geometric factors such as the robot's elastic deformation, and vibration. This will be achieved by integrating real-time error estimation methods with the offline geometric error compensation framework established in the present study.

Supporting information

S1 Table. This table presents the specific data for the pose error of the 5PUS-RPUR parallel robot, as depicted in Fig. 14.
(XLSX)

Author contributions

Formal analysis: Zesheng Wang, Bo Chen.

Funding acquisition: Zesheng Wang, Yanbiao Li, Bo Chen.

Investigation: Bo Chen, Jialong Zhu.

Methodology: Zesheng Wang.

Project administration: Yanbiao Li.

Supervision: Yanbiao Li.

Validation: Bo Chen, Kexin Ding, Jialong Zhu, Min Zhuang.

Visualization: Kexin Ding, Min Zhuang.

Writing – original draft: Zesheng Wang.

Writing – review & editing: Kexin Ding, Jialong Zhu, Min Zhuang.

References

1. Li S, Shan Y, Yu J, Ke Y. Actuation Spaces Synthesis of Lower-Mobility Parallel Mechanisms Based on Screw Theory. Chin J Mech Eng. 2021;34(1). https://doi.org/10.1186/s10033-021-00546-7

2. Ye W, Li Q. Type Synthesis of Lower Mobility Parallel Mechanisms: A Review. Chin J Mech Eng. 2019;32(1). https://doi.org/10.1186/s10033-019-0350-x

3. Chen K, Wang M, Huo X, Wang P, Sun T. Topology and dimension synchronous optimization design of 5-DoF parallel robots for in-situ machining of large-scale steel components. Mech Mach Theory. 2023;179:105105. https://doi.org/10.1016/j.mechmachtheory.2022.105105

4. Chen K, Wang R, Niu Z, Wang P, Sun T. Topology design and performance optimization of six-limbs 5-DOF parallel machining robots. Mech Mach Theory. 2023;185:105333. https://doi.org/10.1016/j.mechmachtheory.2023.105333

5. Ding H, Cao W, Cai C, Kecskeméthy A. Computer-aided structural synthesis of 5-DOF parallel mechanisms and the establishment of kinematic structure databases. Mech Mach Theory. 2015;83:14–30. https://doi.org/10.1016/j.mechmachtheory.2014.08.013

6. Piccin O, Bayle B, Maurin B, de Mathelin M. Kinematic modeling of a 5-DOF parallel mechanism for semi-spherical workspace. Mech Mach Theory. 2009;44(8):1485–96. https://doi.org/10.1016/j.mechmachtheory.2008.11.012

7. He Z, Song Y, Lian B, Sun T. Kinematic Calibration of a 6-DoF Parallel Manipulator With Random and Less Measurements. IEEE Trans Instrum Meas. 2023;72:1–12. https://doi.org/10.1109/tim.2022.3221149

8. Cao L, Liu J, Zhang J, Jiang C, Zhang D. Positioning Accuracy Reliability Analysis of Industrial Robots Considering Epistemic Uncertainty and Correlation. J Mech Des. 2022;145(2). https://doi.org/10.1115/1.4055926

9. Zhang J, Ding F, Liu J, Cao L, Li K. Uncertainty Inverse Analysis of Positioning Accuracy for Error Sources Identification of Industrial Robots. IEEE Trans Rel. 2023;72(3):1123–33. https://doi.org/10.1109/tr.2022.3215673

10. Kong L, Chen G, Wang H, Huang G, Zhang D. Kinematic calibration of a 3-PRRU parallel manipulator based on the complete, minimal and continuous error model. Robot Comput-Integr Manuf. 2021;71:102158. https://doi.org/10.1016/j.rcim.2021.102158

11. Sun T, Lian B, Yang S, Song Y. Kinematic Calibration of Serial and Parallel Robots Based on Finite and Instantaneous Screw Theory. IEEE Trans Robot. 2020;36(3):816–34. https://doi.org/10.1109/tro.2020.2969028

12. Kong L, Chen G, Zhang Z, Wang H. Kinematic calibration and investigation of the influence of universal joint errors on accuracy improvement for a 3-DOF parallel manipulator. Robot Comput-Integr Manuf. 2018;49:388–97. https://doi.org/10.1016/j.rcim.2017.08.002

13. Yin FW, Tian WJ, Liu HT, Huang T, Chetwynd DG. A screw theory based approach to determining the identifiable parameters for calibration of parallel manipulators. Mech Mach Theory. 2020;145:103665. https://doi.org/10.1016/j.mechmachtheory.2019.103665

14. Luo X, Xie F, Liu X-J, Xie Z. Kinematic calibration of a 5-axis parallel machining robot based on dimensionless error mapping matrix. Robot Comput-Integr Manuf. 2021;70:102115. https://doi.org/10.1016/j.rcim.2021.102115

15. Wu L, Yang X, Chen K, Ren H. A Minimal POE-Based Model for Robotic Kinematic Calibration With Only Position Measurements. IEEE Trans Automat Sci Eng. 2015;12(2):758–63. https://doi.org/10.1109/tase.2014.2328652

16. Luo J, Chen S, Fan X, Xiong C, Zheng T, Zhang C, et al. Kinematic Calibration of a 4PPa-2PaR Parallel Mechanism With Subchains on Limbs. IEEE Trans Instrum Meas. 2022;71:1–11. https://doi.org/10.1109/tim.2022.3156998

17. Song Y, Tian W, Tian Y, Liu X. Calibration of a Stewart platform by designing a robust joint compensator with artificial neural networks. Precis Eng. 2022;77:375–84. https://doi.org/10.1016/j.precisioneng.2022.07.001

18. Hu Y, Gao F, Zhao X, Wei B, Zhao D, Zhao Y. Kinematic calibration of a 6-DOF parallel manipulator based on identifiable parameters separation (IPS). Mech Mach Theory. 2018;126:61–78. https://doi.org/10.1016/j.mechmachtheory.2018.03.019

19. Sun T, Zhai Y, Song Y, Zhang J. Kinematic calibration of a 3-DoF rotational parallel manipulator using laser tracker. Robot Comput-Integr Manuf. 2016;41:78–91. https://doi.org/10.1016/j.rcim.2016.02.008

20. Zhang Y, Liu Z, Zheng D, Cai C. The self-calibration method based on grating-rulers used for 6-DOF motion measurement system. Measurement. 2022;204:111894. https://doi.org/10.1016/j.measurement.2022.111894

21. He J, Ding Q, Gao F, Zhang H. Kinematic calibration methodology of hybrid manipulator containing parallel topology with main limb. Measurement. 2020;152:107334. https://doi.org/10.1016/j.measurement.2019.107334

22. Rene EA, Tounsi Fokui WS, Nembou Kouonchie PK. Optimal allocation of plug-in electric vehicle charging stations in the distribution network with distributed generation. Green Ener Intell Transport. 2023;2(3):100094. https://doi.org/10.1016/j.geits.2023.100094

23. Hu YR, Yang SX. A knowledge based genetic algorithm for path planning of a mobile robot. In: 2004 IEEE International Conference on Robotics and Automation (ICRA). 2004, p. 4350–5.

24. Ramirez-Atencia C, Bello-Orgaz G, R-Moreno MD, Camacho D. Solving complex multi-UAV mission planning problems using multi-objective genetic algorithms. Soft Comput. 2016;21(17):4883–900. https://doi.org/10.1007/s00500-016-2376-7

25. Sun P, Li Y, Wang Z, Chen K, Chen B, Zeng X, et al. Inverse displacement analysis of a novel hybrid humanoid robotic arm. Mech Mach Theory. 2020;147:103743. https://doi.org/10.1016/j.mechmachtheory.2019.103743

26. Tang X, Zhou H, Kuang L. Geometric error self-calibration method of five-axis dispensing machine based on the product of exponentials formula. Measurement. 2024;231:114561. https://doi.org/10.1016/j.measurement.2024.114561

27. Li WW, Zhou GB, Zhou XF, Chen ZL, Wu L, Zeng SF. Kinematics analysis of generalized SRU manipulator based on screw theory. In: 2018 3rd International Conference on Robotics and Automation Engineering (ICRAE). 2018; p. 160–5.

28. Bonev IA, Gosselin CM. Analytical determination of the workspace of symmetrical spherical parallel mechanisms. IEEE Trans Robot. 2006;22(5):1011–7. https://doi.org/10.1109/tro.2006.878983

29. Odibat Z, Momani S. Numerical methods for nonlinear partial differential equations of fractional order. Appl Mathemat Model. 2008;32(1):28–39. https://doi.org/10.1016/j.apm.2006.10.025

30. Nubiola A, Bonev IA. Absolute calibration of an ABB IRB 1600 robot using a laser tracker. Robot Comput-Integr Manuf. 2013;29(1):236–45. https://doi.org/10.1016/j.rcim.2012.06.004

31. Zhou C, Fu Y, Ma Y, Han E, He Y, Jiao H. Adjustable Multi-Stream Block-Wise Farthest Point Sampling Acceleration in Point Cloud Analysis. IEEE Trans Circuits Syst II. 2024;71(7):3523–7. https://doi.org/10.1109/tcsii.2024.3364514

32. Wang Z, Li Y, Sun P, Luo Y, Chen B, Zhu W. A multi-objective approach for the trajectory planning of a 7-DOF serial-parallel hybrid humanoid arm. Mech Mach Theory. 2021;165:104423. https://doi.org/10.1016/j.mechmachtheory.2021.104423

33. Thakur M, Meghwani SS, Jalota H. A modified real coded genetic algorithm for constrained optimization. Appl Mathemat Computat. 2014;235:292–317. https://doi.org/10.1016/j.amc.2014.02.093

34. Du G, Liang Y, Li C, Liu PX, Li D. Online Robot Kinematic Calibration Using Hybrid Filter With Multiple Sensors. IEEE Trans Instrum Meas. 2020;69(9):7092–107. https://doi.org/10.1109/tim.2020.2976277

35. Yuan Y, Sun W. An Integrated Kinematic Calibration and Dynamic Identification Method With Only Static Measurements for Serial Robot. IEEE/ASME Trans Mechatron. 2023;28(5):2762–73. https://doi.org/10.1109/tmech.2023.3241302